Desalination and Water Treatment
www.deswater.com
doi: 10.5004/dwt.2023.29527

293 (2023) 49–66
May

LES simulations of a vacuum membrane distillation channel with geometric alterations

Justin Caspar, Guanyang Xue, Alparslan Oztekin*

Department of Mechanical Engineering, Rossin College of Engineering, Lehigh University, Bethlehem, PA, 18015, USA, email: alo2@lehigh.edu

Received 9 November 2022; Accepted 31 March 2023

ABSTRACT

3D LES simulations were carried out to study the performance of a vacuum membrane distillation module. A wiggly wall profile with/without embedded stiffeners was considered to alleviate axial and radial temperature polarization, the cause of performance decrease in membrane distillation. Results of the flow field show the wiggles create unsteady vortex shedding inducing intense mixing in the channel. Vortex shedding intensity increases as the Reynolds number increases or stiffeners are added. 3D results show a 56% improvement in flux when moving from a flat sheet membrane to a wiggly membrane with stiffeners at a constant Reynolds number, corresponding to an improvement from 11.7 to 41.7 in the Nusselt number, showing that the alterations improved the flux performance by enhancing the heat transfer along the membrane surface and therefore alleviating temperature polarization, a critical bottleneck in membrane distillation systems. A merit criterion was defined based on the Nusselt number and friction factor, and a 40% increase in merit was shown switching from a flat to a wiggly channel, while a 97% merit increase was seen going from flat to wiggly with stiffeners. A 42% enhancement in the flux was also seen moving from a straight channel to a wiggly channel at a higher Reynolds number which highlights the importance of strategically choosing the mass flow rate, as well as inducing flow separation and vortex shedding in the channel to promote mixing and dissipate the thermal boundary layer. The variation in results between the wiggly module with stiffeners and the wiggly module at high Reynolds numbers suggests enhancing mixing structures can be more impactful on flux for this geometry than increasing the flow rate to a turbulent/transitional regime. However, both are preferable for peak system flux performance. Furthermore, a 2D approximation was used to perform simulations on more extended channels to examine the length degradation. The modules with wiggly channels performed at the same flux level with a doubling of the length. On the other hand, the flat sheet modules experienced length degradation by temperature polarization and dropped in flux yield by around 13% of the short-channel value. This work illustrates that modeling the system and understanding how the performance decreases as the membrane surface area increases are critical for a larger module (scaling up from a lab to a prototype module) to maintain high flux performance.

Keywords: LES simulations; Computational fluids dynamics; Vacuum membrane distillation; Vortex shedding; Wiggly channel

1. Introduction

Freshwater scarcity is a global issue, and growing industry, population, cities, and more frequent climate events like droughts will exacerbate the problem. It is estimated water demand can exceed supply by 40% in 2030 [1]. The UN Sustainable Development Goals seek to address this via Goal 6: Clean Water and Sanitation. Alternative water

* Corresponding author.

sources, including desalinated and recycled wastewater, are vital for achieving this goal. Recycling wastewater can improve sanitation in growing urban centers and provide a consistent water source in drought, improving resiliency. Desalination plants have already been implemented in 177 countries [2], providing fresh water for 300 million people. Reverse osmosis (RO) is the industry standard for desalination and is also popular for recycling wastewater [3] due to lower operational costs than thermal methods. Recent interest has been focused on other separation methods, such as membrane distillation (MD) or forwards osmosis, to address shortcomings in the reverse osmosis process. Studies claim that successful implementation of membrane distillation can reduce the cost of desalination water from up to \$3.00/m^3 to \$1.17/m^3 [4–6]. There are several factors that ultimately lead to this statement. First, membrane distillation can utilize alternative energy sources such as solar power [7] or waste heat [8] to drive the process instead of using electrical energy to drive high-powered pumps, as in reverse osmosis. Second, fouling has been shown to account for 24% of the operational costs in reverse osmosis [9], and membrane distillation is less fouling-prone than reverse osmosis [10]. The resistance to fouling allows membrane distillation to be applied to a higher range of concentrated solutions [11]. One example is membrane distillation can recover 70%–90% of the water from seawater vs. reverse osmosis at 50% [12]. This will reduce the cost associated with brine disposal and generate more fresh water in a smaller footprint. Other novel techniques are also being considered to reduce the impact of reverse osmosis brine [13], including extracting and using salts for thermal storage, further highlighting the opportunities in brine management.

Membrane distillation is a separation process where a hot feed solution is evaporated near a hydrophobic membrane, and the water vapor passes through the membrane while the liquid solution is prevented from entering the pores because of the hydrophobicity. The vapor layer near the membrane surface provides enhanced fouling resistance. The temperature-driven nature of the process allows membrane distillation to use a larger pore size than reverse osmosis while still achieving theoretically perfect solute rejection. The setup of the permeate channel will vary depending on the type of configuration implemented. Direct contact membrane distillation is the simplest configuration, where the permeate channel flows cold water, condensing the vapor flux [14,15]. The direct contact of cold permeate water with the membrane causes conductive heat transfer through the membrane, reducing the flux performance and energy efficiency [16]. Air gap membrane distillation has a stagnant inert fluid (air) on the permeate side to reduce conductive losses and a cold condenser plate to collect the vapor inside the module [17]. However, the stagnant air causes flux performance losses. This is partially alleviated with flowing gas, leading to the sweeping gas membrane distillation configuration [18,19]. The low specific heat of the air still causes performance losses, but less so than with the stagnant air. The fluid must be condensed external to the module in this configuration, leading to extra costs. A vacuum can be drawn on the permeate side in the vacuum membrane distillation setup, increasing the transmembrane pressure difference [20,21] and creating the highest flux out of all the possible conditions. However, increased pressure differences may cause pore wetting if the liquid entry pressure is exceeded, and the moist air must be condensed externally. In all configurations, membranes can come in flat sheets or hollow fiber shapes. The flat sheet is typically used in a spiral wound module form, and hollow fibers are utilized in a shell-tube arrangement with a high packing ratio. Flux is typically lower in hollow fiber modules due to a lack of mixing in a tighter spacing.

There are still several unsolved issues before membrane distillation becomes a suitable supplement or alternative to reverse osmosis. The first is membrane or pore wetting. If the transmembrane pressure exceeds a specific limit, known as the liquid entry pressure, the feed solution will come into contact with the membrane and can enter the pores. This will compromise the permeate quality and represent a failure of the separation process. Depending on membrane properties, such as pore size, distribution, contact angle, etc., the liquid entry pressure can vary, where measured values of the entry pressure range between 100 to 500 kPa [22,23]. Wetting and fouling are highly correlated in membrane distillation systems [24]. Fouling of specific compounds such as gypsum occurs more rapidly as the temperature increases, another issue in the presence of hot feed solutions [25]. In addition, similar to concentration polarization in reverse osmosis, temperature polarization in membrane distillation can substantially influence the flux. Temperature polarization occurs near the membrane surface as heat is removed from the fluid to supply the heat of evaporation [26]. As the local membrane temperature decreases, so will the vapor flux. Note that concentration polarization can also occur but doesn't have the same impact on the flux as temperature polarization in the absence of fouling. Researchers attempt to reduce the effect of polarization near the membrane surface by promoting mixing in the channel. In particular, spacers or other flow obstructions are commonly used [27,28] to generate vortices and other mixing structures that improve the overall module performance.

Back in the 1990s, Schofield et al. theoretically showed applying a vacuum can increase the flux performance of membrane distillation [29]. Li et al. conducted experiments in the vacuum configuration using hollow fiber membranes [30] for several commercially available membranes with different operational conditions. Results showed that increasing the Reynolds number helped reduce the temperature polarization in the module and led to a higher flux. Kim et al. [31] performed a theoretical study on vacuum membrane distillation and direct contact distillation in hollow fibers by studying the Knudsen and Brownian components of vapor diffusion through the membrane. It was found for the vacuum systems that the Knudsen component dominates the flux, but that molecule-molecule collisions (Brownian) shouldn't be ignored. Soni et al. created a model to study VMD and experimentally validated it [32] using a mixture of water and ethanol. Ji et al. conducted vacuum membrane distillation experiments using a hollow fiber module [33] at 64 g/kg concentrations, corresponding to reverse osmosis brine, and observed no wetting. Zhang et al. [34] showed VMD flux increasing with feed temperature and inlet flow rate. Wang et al. designed and tested a solar-thermal VMD module with artificial seawater. For an inlet temperature of

343 K, a flux value of 13 kg/m^2·h was reported with a vacuum pressure of 10 kPa, and the flux declined near 0 as the vacuum pressure was increased towards 60 kPa [35]. Current experimental trends in the vacuum membrane distillation field include testing a multi-effects module [36]. Pure water production is traded for increased energy efficiency by recovering heat from the vapor flux [37,38]. Similar heat recovery has also been implemented for direct contact membrane distillation [39].

In the CFD studies, many authors studying membrane distillation configurations, in general, are using several strategies to promote mixing and improve performance. For example, Gruber et al. used OpenFOAM to study spacer geometries [40] and concluded that denser spacers resulted in higher flux. Next, Gruber et al. extended the geometry considered to model experimental conditions more realistically and showed a validation between CFD and numerical results for various flow rates [41]. Alwatban et al. [42] observed a 40%–55% increase in vapor flux when spacers were added to a DCMD flat sheet channel, depending on the arrangement of spacers. Anqi et al. [43] studied the effect of operating conditions with and without spacers using LES simulations for a VMD setup. They observed a substantial increase in the flux using spacers at increased feed flow rate and temperature. Amigo et al. used a laminar flow model in OpenFOAM combined with a MATLAB postprocessing technique to show fouling-prone regions in a DCMD module with and without spacers [44]. In addition, researchers also consider membrane morphology changes such as corrugations and other surface patterns [45–48]. For example, a 30% increase in flux was found for corrugated RO membranes compared to a flat sheet membrane. Gryta arranged hollow fiber membranes without an external housing in various configurations, from a typical parallel arrangement of fibers to a U-shaped module using nets to support the fibers. The permeate flux increased as mixing was introduced into the feed tank using a magnetic stirrer [49]. Mericq et al. conducted experiments to validate a simulation model that was then used to determine the system's performance vs. various operational conditions, such as vacuum pressure, inlet feed temperature, and Reynolds number for various membrane properties. The specific energy was lowest at low temperatures, although the permeate flux was highest at elevated temperatures. The specific energy was primarily dominated by the component required to heat the feed water [50]. Tiwari et al. [51] also utilized geometric alterations by creating a U-bend inside a thin pipe to induce secondary flows via curvature in the laminar flow regime and showed the presence of vortex activity inside the flow channel, which directed particles away from the membrane and mitigated the effect of gravity-driven settling. Another scenario where secondary flows can be considered is through natural convection, which has been shown to improve heat transfer characteristics in classical cases, such as flow around a cylinder or flow over a flat plate by generating convection cells that increase the heat transfer coefficient between the fluid and solid [52,53].

While CFD studies are a useful design tool, other research topics are also considered to improve membrane distillation performance. Membrane manufacturing methods such as adding carbon nanotubes (CNTs) to membranes [54], utilizing hydrophobic/hydrophilic composite membranes [55], and creating superhydrophobic membranes [27,56]. Flow through CNTs is low friction and, therefore, can achieve a much higher flux than conventional membranes while separating all required molecules. This can increase the energy efficiency of desalination. Molecular dynamics simulations are a valuable tool for characterizing flow performance through CNTs [55], which test different nanotube configurations and the diameter to find one best suited for desalination applications.

Xie et al. [57] study the effect of various sinusoidal channel profiles on the performance of a reverse osmosis setup. Results showed that the wiggly channel outperformed a channel with net-type spacers. Ling et al. applied various fouling models to study 144 geometries consisting of membrane morphology changes – varied from the shape of the sine curve – and topographical changes – such as different spacer layouts [58]. They showed topographical alterations (spacers) were more effective at increasing the flux performance than changing the channel's curvature at higher flow rates. This behavior was flipped at low Reynolds numbers. Their models proved to be accurate compared to the experiments.

Scaling up membrane modules is essential for industrial applications of this technology. Winter et al. [59] designed and fabricated several prototype scale modules of different membrane surface areas and tested them in the permeate gap configuration – optimized for heat recovery and the maximize the specific production value of pure water. As the membrane surface area increased from 5 to 15 m^2, the flux decreased from 7.5 to 5 kg/h. Similar results were seen in another of their experiments [60], wherein a direct contact membrane distillation module, as the channel length increased from 1 to 7 m, the specific flux decreased from 14 to 3 kg/m^2·h. Another pilot study was conducted for an air gap membrane distillation module using heat generated from a solar plant, Plataforma Solar de Almería, in Spain [61] on a 2.8 m^2 membrane module over 4 months of testing. A flux of 6.51 L/m^2/h was reported at peak operating conditions, with a 14% decrease as the salinity of the feed solution increased. The test module encountered issues with leakage around the membrane seal and wetting at high feed solution conductivities, showing that scaling up membrane modules from lab to prototypes can be very challenging. Currently, prototype modules are heavily designed to consider heat recovery to bring down the \$/m^3 of water. Thomas et al. constructed a pilot module [62] with four stages, each around 4.0 m^2, with the feed solution heated through a solar array. A module flux performance of 11.0 L/m^2/h was observed with seawater as the feed solution. Another 4 m2 pilot study was conducted in Tunisia under Gabsi et al. in the vacuum membrane distillation configuration [63,64] with the feed solution heated using solar energy. A maximum flux of 21.0 L/h was observed around mid-day in March when the solar radiation peaked. The authors reported a much higher flux in June of 70 L/h with higher radiation. The Reynolds number for the feed solution was in the laminar regime, 670, and was variable depending on the available solar heat. Duong et. Al. also studied a pilot membrane distillation module with a surface area of 7.2 m^2 [65] with a design optimized

for the heat recovery of the latent heat of the permeate stream. RO brine was used as the feed solution with a concentration of 8,000 mg/L of sodium chloride, and flux of 16 L/h was achieved at the highest flow rate and temperature considered in the study with a rejection rate consistently above 99%, showing how membrane distillation is a valuable tool for treating high salinity solutions.

CFD is a valuable tool to gauge system performance for a wide range of parameters in membrane distillation modules containing sinusoidal ("wiggly") membranes with and without embedded stiffeners. Similar geometries have only been considered in reverse osmosis in a slightly different layout. The flow and temperature field should be resolved to the highest accuracy for the computational model to be consistent with experimental conditions. The current study utilizes the large eddy simulation (LES) turbulence model in 3D to conduct simulations at a turbulent Reynolds number. To the best of the authors' knowledge, this is a gap in the existing literature for membrane distillation. The local surface temperature, vapor flux, and solution concentration are fully coupled, using no empirical relationships for the heat transfer. The chosen configuration is vacuum membrane distillation based on the high flux potential compared to other configurations.

2. Mathematical model

OpenFOAM v2012, an open-source C++ library, is used to solve the governing equations for the VMD process. The swak4foam library was used to implement the membrane boundary condition. In addition, PimpleFoam, a transient, incompressible solver for the flow field, was modified to include the temperature and concentration scalar transport.

The continuity equation:

$$\frac{\partial U_i}{\partial t} + \frac{\partial U_i}{\partial x_i} = 0 \tag{1}$$

where U_i is the velocity field written in the tensor form and x_i is the Cartesian coordinate (x,y,z), the time coordinate is t. The unsteady conservation of momentum equation is:

$$\frac{\partial U_i}{\partial t} + U_j \frac{\partial U_i}{\partial x_j} = -\frac{\partial \tilde{p}}{\partial x_i} + \nu \frac{\partial}{\partial x_j}\left(\frac{\partial U_i}{\partial x_j}\right) \tag{2}$$

where ν is the kinematic viscosity of the fluid and the kinematic pressure $\tilde{p}$ represents p/ϱ. The Navier–Stokes equations shown above can be solved for the pressure and velocity field. The energy and mass transport equations are shown below as convective–diffusive equations:

$$\frac{\partial T}{\partial t} + U_j \frac{\partial T}{\partial x_j} = D_T \frac{\partial}{\partial x_j}\left(\frac{\partial T}{\partial x_j}\right) \tag{3}$$

and

$$\frac{\partial c}{\partial t} + U_j \frac{\partial c}{\partial x_j} = D_c \frac{\partial}{\partial x_j}\left(\frac{\partial c}{\partial x_j}\right) \tag{4}$$

where T is the temperature scalar, and c is the concentration scalar. D_c is the mass diffusivity, and thermal diffusivity is taken as $D_T = k_f/(\varrho\, c_p)$, where k_f is thermal conductivity, and c_p is specific heat. Note that all material properties are held constant. Because turbulent structures are present in the channel at high Reynolds numbers, the LES turbulence model with WALE sub-grid scheme was considered to capture the unsteady flow; see the supplement for details on turbulence modeling.

Shown below are the coupled boundary conditions for membrane distillation modeling. The hydrophobic membrane cannot allow the feed solution to enter the pores for the separation process to function correctly. This is achieved by ensuring that the pressure exerted on the membrane surface does not exceed the membrane's liquid entry pressure (LEP). The Young–Laplace equation defines the pressure as a function of the membrane properties:

$$\mathrm{LEP} = \frac{-2\cos(\alpha) B \gamma_l}{r_{\max}} \tag{5}$$

where B is the geometric factor determined by pore structure, γ_l is the liquid surface tension, α is the liquid–solid contact angle, and $r_{\max}$ is the largest pore radius.

The two mechanisms driving the VMD process are the partial vapor pressure of the feed at the membrane surface and the vacuum pressure. The partial vapor pressure of the feed is a function that increases with increasing temperature and decreasing concentration. The partial pressure of water vapor in the binary mixture is determined from:

$$p_{\mathrm{wf}} = y_w p = X_w \alpha_w p_w^0 \tag{6}$$

where p_{wf} represents the partial pressure of water vapor on the feed side, y_w and X_w are the vapor and liquid mole fractions of water, respectively, p is the total pressure of the mixture, and p_w^0 is the saturation pressure of pure water, determined by the Antoine equation. α_w is the activity coefficient of water in NaCl solutions determined by Schofield [66] shown below, where X_{NaCl} scales linearly with the solution concentration, c, by a factor of the molecular weight of the solvent, sodium chloride, in this case. The Antoine equation to determine the partial vapor pressure for the ideal mixture on the feed side is:

$$\alpha_w = 1 - 0.5X_{\mathrm{NaCl}} - 10X_{\mathrm{NaCl}}^2 \tag{7}$$

$$p_w^0 = \exp\left(A - \frac{B}{C+T}\right) \tag{8}$$

where A, B, and C constants for water are given as A = 23.1964, B = 3816.44, and C = 46.13 [67] for a temperature in Kelvin.

The dusty gas model (DGM), shown in Lawson and Lloyd [68], describes mass (vapor) transfer in membrane distillation using three mechanisms: Knudsen (molecule-wall collisions) diffusion, molecular (molecule-air collisions) diffusion, and viscous (molecule-molecule collisions) diffusion.

Molecular diffusion is neglected for VMD since the vacuum removes the air from the membrane pores. The Knudsen number determines which mechanism is dominant, and the calculation is shown in the equation below as the ratio of the pore size, r_p, to the mean free path λ. The expression for the mean free path is given as [69,70]:

$$\lambda = \frac{k_B T}{\bar{p}\pi\sigma^2\sqrt{2}} \tag{9}$$

where σ is the collision diameter of the water molecules, $\bar{p}$ is the mean pressure within the membrane pores, T is the absolute temperature, and k_B is Boltzmann's constant. For the present study, the Knudsen number is calculated to be 2.78. Note that pressure is a function of temperature, which heavily influences the Knudsen number. The parallel circuit connection of Knudsen and Viscous diffusion is considered at Knudsen numbers between 0.01 and 10. At any Knudsen number over 10, it is assumed only Knudsen diffusion will appropriately model the vapor transport. Having a Knudsen number greater than 1.0 means the Knudsen flux component will dominate over the viscous component (in post-processing, it was found that the Knudsen component contributed over 95% of the vapor flux).

For the current study, the Knudsen and the viscous mechanism need to be considered to describe the mass transfer through the membrane. The total molar flux of water vapor can be expressed as the sum of Knudsen, J_k, and viscous diffusion J_v, so $J_t = J_k + J_v$ [43,71]:

$$J_k = \frac{2\varepsilon_s r_p}{3\tau RT\delta}\sqrt{\frac{8RT}{M_w\pi}}\left(p_{\mathrm{wf}} - p_v\right) \tag{10}$$

$$J_v = \frac{\bar{p}\varepsilon_s r_p^2}{8\tau\delta RT\mu_w}\left(p_{\mathrm{wf}} - p_v\right) \tag{11}$$

where r_p is the pore radius, τ is membrane tortuosity, δ is membrane thickness, R is the universal gas constant, T is local temperature, M_w is the molecular weight of water, μ_w is water vapor viscosity, $\bar{p}$ is the mean pressure within the membrane pores, p_{wf} is the partial pressure of the water vapor in the feed side of the membrane pores, and p_v is vacuum pressure at the permeate side of the membrane pores. The surface porosity, $\varepsilon_s = \varepsilon/\tau$, can be determined as a function of porosity and tortuosity [72].

To finish the coupling between flux and temperature, the thermal boundary conditions are given below, where Q_m is the heat flux through the membrane:

$$Q_m = N_t \times \Delta h_{\mathrm{fg}} \tag{12}$$

$$\Delta h_{\mathrm{fg}} = 3{,}177{,}800 - 2{,}464T \tag{13}$$

where $N_t = J_t M_w$ is the total mass flux, M_w is the molecular weight of water, and Δh_{fg} is the specific enthalpy of water vaporization. The conductive heat flux through the membrane is neglected due to the presence of the vacuum, which effectively works as a thermal insulator.

2.1. Numerical set-up

2.1.1. Geometric parameters

The current study compares the performance of several vacuum membrane distillation modules using 3D LES simulations for a length of 90 mm. Results were then compared against a 2D model, and there was no appreciable difference in flux between 2D and 3D simulations. Therefore, 2D LES simulations were run on VMD modules with a length of 170 mm, where the 3D model would be computationally expensive to consider. While there is skepticism regarding 2D LES simulations [73], the reduction in filtering in LES vs. RANS models should prove a reasonable assumption to increase the channel length without the massive computational expense, as shown in later figures.

Three different channel configurations are shown in Fig. 1. The base case (bottom) is a flat sheet membrane with a height H of 2 mm and a length L of 97 mm, or 48.5H. Applying a sinusoidal profile to the wall height creates the geometry shown on the top, where the length is reduced to 45H to keep the membrane surface area (arc length) constant. There is an x/H of 5.0 flat section at the beginning and end of the curve so the flow can develop, which assists the convergence of the solution. The local maxima and minima of the sine curve are highlighted, and one occurs every x/H of 5.0 starting from x/H of 7.5, giving the sine curve a frequency of 20 mm, or x/H of 10, shown in the height function. Stiffeners are embedded into the membrane in the middle geometry to provide additional structural support and turbulent mixing. The stiffener strands have a diameter of 0.8 mm or x/H of 0.4. All cases in Fig. 1 have a width of x/H of 2.5 or 5.0 mm.

All cases utilize a structured mesh with good orthogonality and a minimal aspect ratio. Zoomed-in images of the mesh are presented in Fig. 2. The top image is for the wiggly case without stiffeners, and the bottom includes the stiffeners. These meshes were generated using ANSYS Fluent 2021 R1. The flat sheet meshes were built using the blockMesh function in OpenFOAM. There is grading near the membrane surface to capture the concentration and

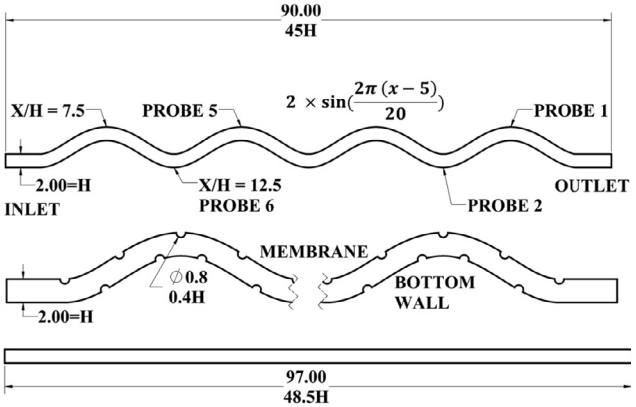

Fig. 1. The side view of the computational domain for both the wiggly (with and without stiffeners) and flat sheet membrane. Dimensions in mm. The membrane surface area is kept constant. Drawing with embedded stiffeners magnified to show greater detail. Width is 5.0 mm, z/H = 2.5.

thermal boundary layer in the wiggly case and grading near the membrane surface and bottom wall in the case with stiffeners to accurately resolve additional turbulence imposed and ensure an adequate $y+$ value. For all cases, the average $y+$ value on the membrane surface is 0.5, while the average $y+$ value for the bottom wall is 2.2 or 1.75, depending on the case, showing the mesh is suitable for LES simulations.

A mesh dependency study was conducted for the wiggly mesh, with four different densities from 10 to 33 million elements. Time-averaged 2D line plots of flux and concentration over the membrane surface are presented after 3.0 s of flow time. The results from Fig. 3 show a mesh density of 20 million cells ensures mesh independency. This is based on the normalized concentration, which is most sensitive to the number and quality of elements near the membrane. For example, at x/H of 5.0–10.0, there is a difference in concentration profiles from 15 to 20 m cells, and there isn't one between 20 to 33 m cells, demonstrating the concentration boundary layer near the membrane surface is grid-independent. Note that the average flux is consistent for all four meshes, even though there is local variance near the beginning of the flow channel based on the different concentration levels. Also, the mesh density will affect the transient behavior of the simulation. These simulations were run on the module without stiffeners. The geometry with stiffeners utilized a mesh with 33 million finite volume cells to account for the additional induced turbulent structures in the channel.

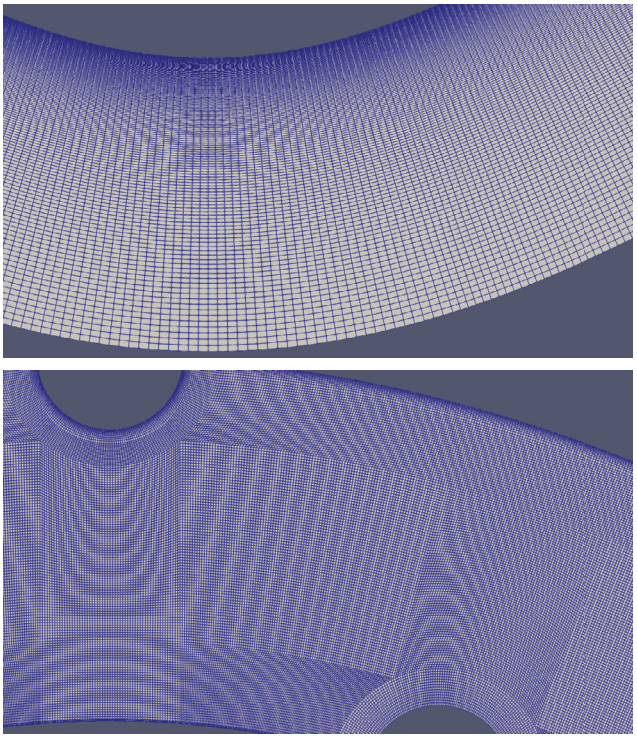

Fig. 2. Zoomed-in images of the mesh for the (top) wiggly case and (bottom) wiggly with embedded stiffeners case.

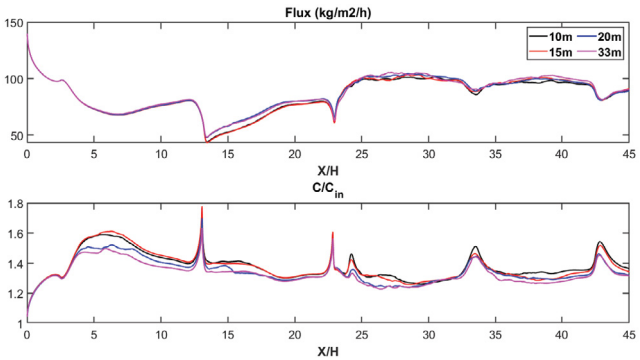

Fig. 3. Time-averaged 2D line plots along the membrane surface of (top) flux and (bottom) normalized concentration at four different mesh densities.

Fig. 4 shows line plots of the normalized temperature collected at four different probe locations vs. time for the first 2.5 s of flow time at Re = 1,500 for the wiggly case. Probe data shows that the behavior in the channel has reached a quasi-periodic state from the initial conditions, and that any time greater than 2.5 s is sufficient to capture unsteady structures in the channel. Probes are labeled in Fig. 1. The flow near the outlet shows a high density of mixing structures and vorticity compared to the inlet region. Based on the data, the mixing time scale is much shorter than the amount of simulated flow time. Therefore, the LES model for over 2.5 s of flow time is sufficient to capture the behavior in the channel.

Probes 1 and 2 are placed in the well-mixed regime near the outlet, whereas probes 5 and 6 are in the non-mixed region. The data obtained by probes 1 and 2 show very little sensitivity to the end time of the simulation on the temperature along the membrane. There is a periodic vortex shedding at the site of probes 5 and 6. The vortex forms and grows in time and sheds. A burst of smaller eddies occurs when the vortex is shedding, and eddies dissipate rapidly. The patterns displayed in Fig. 4 result from the periodically repeated vortex activities in this region. Smaller eddies aid in very effective mixing, causing temperature polarization to decrease sharply near probes 5 and 6, shown by T/T_{in} approaching 0.98 or higher and gradually decreasing

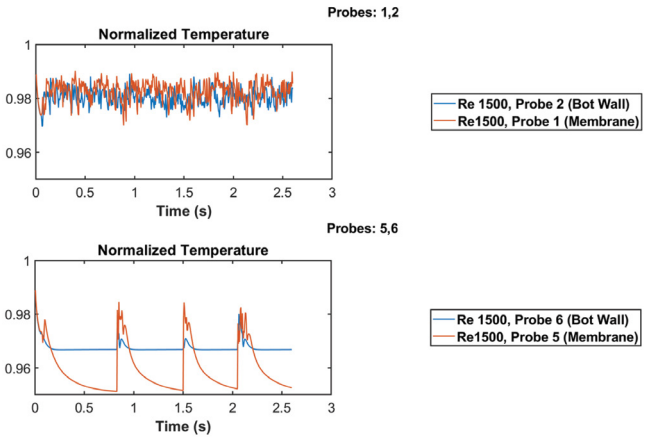

Fig. 4. Probe data of normalized temperature for (top) probe locations 1 and 2 and (bottom) probe locations 5 and 6 to highlight the appropriate selection of the simulation end time.

as eddies dissipate. Since there aren't dramatic changes in behavior as time increases and based on the quasi-periodicity of the data, the authors have chosen 3.0 s as the end time. For all simulations, adaptive time-stepping was used to keep the maximum Courant number below 1.0.

2.1.2. Validation

Results from the validation study are shown in Table 1. There is good agreeance with experimental results at Reynolds number 1,000, and more error is introduced at Reynolds number 200. The results are conducted on a flat sheet membrane channel, with the operational parameters specified in Table 1. The experiments used to conduct the validation study are referenced in [43]. The close agreement with experimental results for the flux values highlights the model's validity in predicting the flux behavior for VMD systems. The high error value at low Reynolds numbers can correspond to a mismatch between experimental and CFD conditions; for instance, adjustable speed pumps can enter a transient flow regime if operated far outside the design point. Another source of error includes the translation of membrane properties into CFD modeling; for instance, commercial membranes have a variation in properties from the manufacturing process, and the CFD model considers a constant pore size instead of a variable distribution as all membranes have. The validation of this model closely followed the study of the corresponding author's previous studies [43,74]. However, the validation was redone since this model's implementation differs from previous studies. A good result was found with experimental data at Reynolds number 1,000 in a flat sheet module, with a 1.1%–4.4% error based on the inlet temperature.

2.1.3. Operational conditions

Table 2 shows the operational conditions, fluid, and membrane properties for the simulation. The feed fluid properties are chosen to represent hot seawater as a binary mixture of sodium chloride and water. The membrane properties are taken from commercial flat sheet membrane values used for vacuum distillation systems [30]. The vacuum pressure is also chosen based on experimental studies cited in the literature review section. Alongside the various geometrical configurations considered, each is run at two different Reynolds numbers (Re = $U_{in}D/v$) 1,500 and 2,500, with the inlet velocity corresponding to 0.75 and 1.25 m/s. One Reynolds number is in the laminar regime, and the other is in the transitional flow regime where turbulent structures are expected. The height of the channel (2 mm) is taken as the characteristic length.

As shown below and in the mathematical modeling, the membrane surface is treated as a coupled boundary condition between the mass flux (velocity), temperature, and concentration field. In the table, the arrow denotes a vector quantity, and $\vec{n}$ is the positive outwards normal direction, that is, $\overrightarrow{V_n}$ is the normal velocity component, and ∂_n is the normal gradient. In all cases, the unit normal vector varies based on the location along the sine curve. The normalized temperature, velocity, and concentration values are presented in the results section. All quantities are normalized with the inlet value (Table 2). The normalized temperature and concentration can also represent the polarization coefficients in the vacuum distillation model, treated as a single-channel flow system. The normalization scheme, X/X_{inlet}, where X represents any data quantity (velocity, temperature, etc.) The polarization coefficient can drastically change the system's performance and will be examined in depth.

Additional non-dimensional parameters are used to characterize the system performance. The Prandtl and Schmidt numbers are calculated based on the kinematic viscosity and the thermal and mass diffusivity coefficients. The formulation for the two is shown below:

Table 2
Operational conditions considered for the present work

Parameters	Values
Pore diameter, d_p	0.2 (μm)
Porosity, ε	80% (–)
Thickness, δ	150 (μm)
Tortuosity, τ	1/ε (–)
Vacuum pressure, p_v	5,000 (Pa)
Kinematic viscosity, ν	1e-6 (m^2/s)
Thermal diffusivity, D_T	1.5e-7 (m^2/s)
Mass diffusivity, D_C	1.5e-9 (m^2/s)
Prandtl number	6.67 (–)
Schmidt number	667 (–)
Feed inlet temperature, T	353 (K)
NaCl inlet concentration, c	35 (kg/m^3)
Reynolds number, Re	1,500; 2,500

Table 1
Validation study results

Channel dimension: width = 15 mm, L = 7.0 mm, h = 3 mm					
Properties: ε = 0.8, δ = 100 μm, pore diameter = 0.2 μm, τ = 1/ε, P_{vac} = 5,000 Pa					
T_{in}	Re	Feed velocity (m/s)	Experimental flux ($kg/m^2 \cdot h$)	Numerical flux ($kg/m^2 \cdot h$)	Percent difference (%)
50°C	200	0.04	11.6	15.6	25
	1,000	0.19	19.7	20.6	4.4
80°C	200	0.026	42.8	37.4	14
	1,000	0.122	57.3	56.7	1.1

$$\mathrm{Pr} = \frac{\nu}{D_T} \tag{14}$$

$$\mathrm{Sc} = \frac{\nu}{D_C} \tag{15}$$

The Prandtl number of the flow is 6.67, and the Schmidt number is 667. Note the Prandtl number is approximately scaling with Schmidt$^{1/3}$. These show the relative magnitude of the thermal/mass diffusion in the system vs. the momentum diffusion. Since both numbers are greater than unity, the corresponding boundary layers will be thinner than the momentum boundary layer. This is especially notable in the Schmidt number, two orders of magnitude greater than 1.0, highlighting a small concentration boundary layer. Therefore, the contours presented will ignore concentration since the gradient is challenging to visualize in contour format, and line plots over the membrane are a more useful tool. Additionally, line plots of the Nusselt and Sherwood numbers are also presented, where the formulation for the corresponding non-dimensional analysis and treatment of the heat/mass transfer coefficient are shown below:

$$\mathrm{Nu} = \frac{h_{\mathrm{thermal}} L}{k_f}; h_{\mathrm{thermal}} = \frac{k_f \dfrac{\partial T}{\partial \vec{n}}}{T_{\mathrm{membrane}} - T_{\mathrm{bulk}}} \tag{16}$$

$$\mathrm{Sh} = \frac{h_{\mathrm{mass}} L}{D_C}; h_{\mathrm{mass}} = \frac{D_C \dfrac{\partial C}{\partial \vec{n}}}{C_{\mathrm{membrane}} - C_{\mathrm{bulk}}} \tag{17}$$

where the heat transfer coefficient is post-processed by rearranging the boundary condition, $k_f \frac{\partial T}{\partial \vec{n}} = h_{\mathrm{thermal}} \left(T_{\mathrm{membrane}} - T_{\mathrm{bulk}} \right)$ to solve for the transfer coefficient. The temperature gradient along the membrane surface is calculated as part of the solution. Note how in Table 3, the heat flux through the membrane scales linearly with the vapor flux, $k_f \frac{\partial T}{\partial \vec{n}} = N_t \times \Delta h_{\mathrm{fg}}$, so the convective heat transfer coefficient and corresponding Nusselt number is another way of reframing the flux performance of the system in a non-dimensional form. Finally, having calculated the temperature gradient and membrane temperature OpenFOAM solution, the bulk temperature is post-processed using volume averaging throughout the channel in increments of $x/H \sim 0.1$. The friction factor for each case is post-processed from the pressure drop and other simulation parameters, where the formulation for the friction factor is shown below. Additionally, a dimensionless merit criterion is defined below as the ratio of the Nusselt number and friction factor. If the merit criterion is greater than one, it means there is an increase in the heat transfer performance of the system greater than the increase in frictional factor throughout the module.

$$f = \frac{\Delta P D}{L\left(\rho U_{\mathrm{in}}^2 / 2\right)} \tag{18}$$

$$\mathrm{Merit} = \frac{\left(\mathrm{Nu} / \mathrm{Nu}_{\mathrm{ref}}\right)}{\left(f / f_{\mathrm{ref}}\right)^{1/3}} \tag{19}$$

3. Results and discussion

CFD studies used the LES turbulence model to resolve the flow inside a vacuum membrane distillation module in various geometric configurations. Using flow obstructions like spacers or corrugations at high flow rates induces mixing structures, increasing performance. The present study aims to consider the effect of changing the channel geometry to introduce vortex activity through various geometrical alterations, including a wiggly channel and a wiggly channel with embedded stiffeners.

Fig. 5 shows contours for the sinusoidal/wiggly channel at Reynolds number 1,500. The grid lines highlight x/H values along the length of the channel. Contours are zoomed in between x/H 15.0 and 45.0 to provide further clarity. Note concentration isn't shown since the boundary layer is very thin and hard to capture in contours, but it will be discussed in tables and line plots. The top contour shows normalized velocity magnitude. Here there are two district regions inside the flow field. The velocity profile is parabolic in the upstream area, closer to the inlet, with no mixing structures. There is a large momentum boundary layer along the bottom wall and the membrane, where the thickness of the boundary layer changes as the bulk fluid is re-directed by the curvature of the channel. The boundary layer is thicker at x/H of 17.5 and thinner at x/H of 22.5. There is no vortex shedding near the inlet, and the boundary layer is attached. This is shown in the contours of normalized temperature, where a noticeable thermal boundary layer is at the membrane

Table 3
Boundary conditions for the flat and wiggly case. Note a no-slip/no-penetration condition is applied to all the embedded stiffeners. The side walls use a symmetry boundary condition where the normal gradient of the field is set to 0

Patch name	U (m/s)	$\tilde{p}$ (m^2/s^2)	T (K)	C (kg/m^3)
Inlet	$\overrightarrow{V_n} = U_{\mathrm{in}}$	$\partial_n = 0$	T_{in}	C_{in}
Outlet	$\partial_n = 0$	0	$\partial_n = 0$	$\partial_n = 0$
Membrane (top surface)	$\overrightarrow{V_n} = \frac{N_t}{\rho}$	$\partial_n = 0$	$k_f \frac{\partial T}{\partial \vec{n}} = N_t \times \Delta h_{\mathrm{fg}}$	$D_c \frac{\partial c}{\partial \vec{n}} = N_t \times c$
Bottom surface (wall)	No-slip/penetration	$\partial_n = 0$	$\partial_n = 0$	$\partial_n = 0$

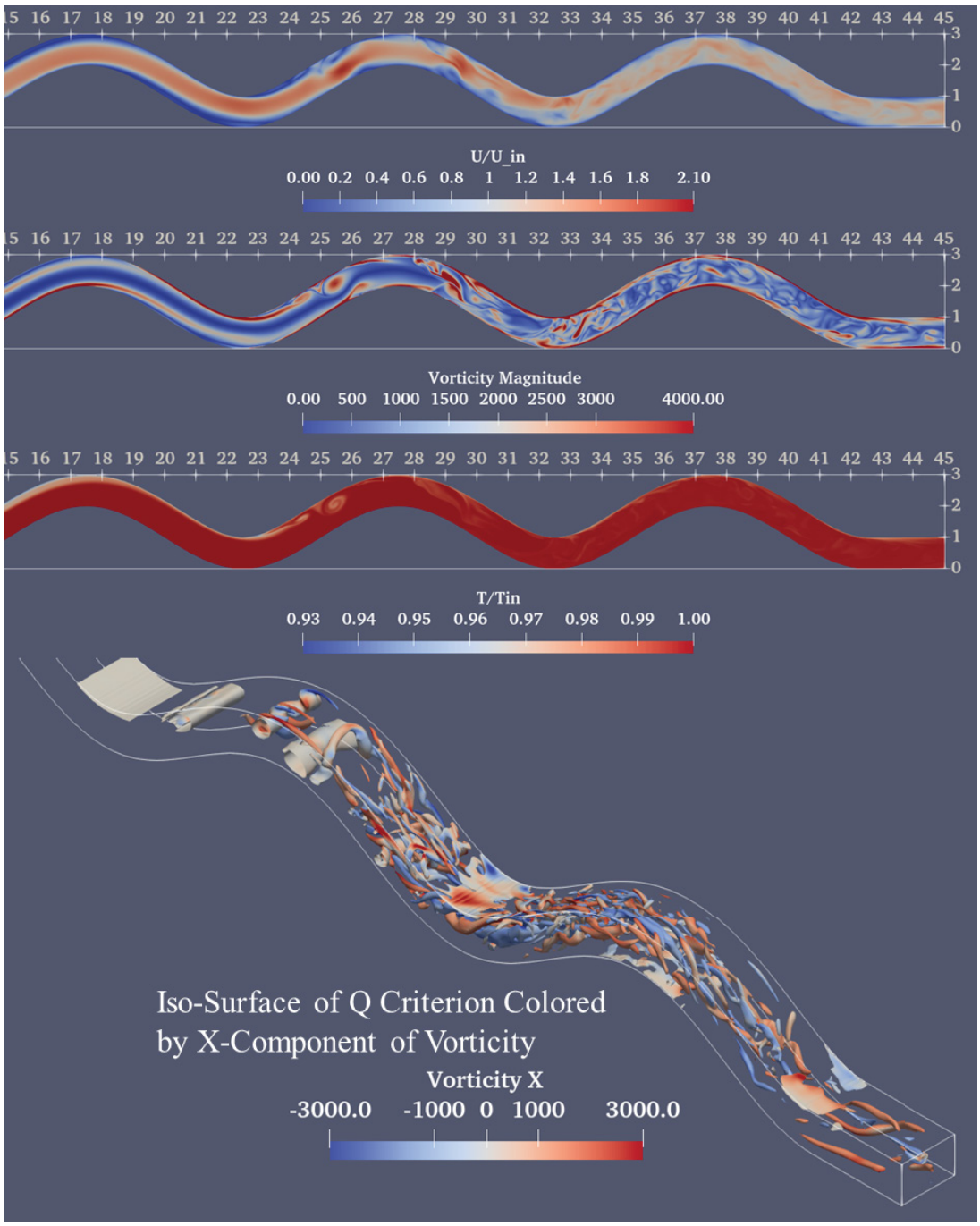

Fig. 5. Midplane contours of (top) normalized velocity (middle) vorticity magnitude (bottom) normalized temperature for Re 1,500 with a sinusoidal channel profile. Midplane corresponds to $z/H = 1.25$.

surface. Again, the boundary thickness changes as the fluid is redirected (the momentum and thermal boundary layer structure show similar behavior).

A transition in the flow field occurs at x/H of 22.5. Where, downstream, mixing structures are present in the channel, and vortex shedding begins. This is shown in vorticity contours, where rotational structures begin at x/H of 22.5 to 27.5. These structures have a vorticity component only around the Z-axis. Further downstream of this region, the organized vortex structures are broken into more chaotic vortex filaments. This is shown in the bottom image containing the iso-surface of the Q-Criterion. Iso-surfaces are colored by the vorticity component along the x-direction to show counter/clockwise rotational direction. The rolling vortices near the origin of the shedding have no in-out-of-plane rotational component, while the filaments do. The mixing effect is seen in the contours of normalized temperature, where areas of high vorticity magnitude and disorganized mixing structures

reduce the thickness of the thermal boundary layer near the membrane by reintroducing the hotter bulk fluid, causing the membrane to have a higher local temperature. The velocity field in the mixed region shows the dissipation of the momentum boundary layer upon which the thermal boundary layer thickness is based. From the structures of the vortices and corresponding normalized temperature values, the dis-organized structures were more effective at reducing the thermal boundary layer thickness. A reduced boundary layer thickness leads to an enhanced heat transfer coefficient near the membrane and higher bulk temperatures. More heat can be supplied to combat the losses through local evaporation and achieve higher flux performance.

The probe data presented in Fig. 4 also highlights the effect of mixing. Probes 1 and 2 are placed in the well-mixed area of the channel nearest to the outlet, while Probes 5 and 6 are placed much closer to the inlet in the unmixed region. First, looking at the data corresponding to the line plots on the membrane surface, probe 1 (mixed region) shows a higher temperature than probe 5 (unmixed region), corresponding to a much higher flux value. The mixing effect is also seen between the membrane and the bottom wall. In the case of Probe 5 and 6 in the unmixed region, since the bottom wall is a fully insulated surface instead of a membrane, the local temperature is much higher than the upper membrane surface. This shows the effect of radial temperature polarization in the channel corresponding to the thermal boundary layer. However, with Probes 1 and 2, the two temperatures are equilibrated, showing the vortex structures are dissipating the boundary layer and providing a more evenly distributed temperature throughout the channel. When the vortex shedding occurs at probes 5 and 6, the temperature dramatically increases and causes the flux performance to increase.

Fig. 6 shows the contours and iso-surfaces for Reynolds number 2,500. While this is in the transitional flow regime, the LES turbulence model should be sufficient to resolve the structures. One significant difference between the two cases is the transient structures begin closer to the inlet, where vortex activity begins at x/H of 17.5 for Reynolds number 2,500 compared to x/H of 22.5 for Reynolds number 1,500. In terms of the channel geometry, this means shedding begins at the previous corner of the channel. In all wiggly cases, flow separation and vortex shedding begin at one of the turning corners in the channel. The larger region of high vortex activity can be seen in the normalized velocity and vorticity magnitude contours. In addition to an increase in the size of the mixed portion of the flow field, the vorticity magnitude is also greater at Reynolds number 2,500, where larger areas show the highest value than the Reynolds number 1,500 case. The effect of the enhanced mixing can also be seen in the normalized velocity and temperature contours where the momentum and thermal boundary layer are further confined to the wall, and membrane boundary layers are vastly reduced in size, almost to the point where it's hard to visualize based on the contours (to keep the color scale consistent between figures some resolution is lost in the Reynolds number 2,500 contours).

In addition to a larger vorticity magnitude, further reduction in temperature polarization, and increased length of the vortex-dominated (mixed) regime in the flow field, there is also a change in the vortex filaments' structures. The iso-surfaces of the Q-criterion show the filaments are packed more densely in the case with more mixing, and more of those filaments have a higher vorticity in the Reynolds number 2,500 case compared to Reynolds number 1,500.

The final point of comparison for the geometry presented in Fig. 1 is below for Re = 1,500 with embedded stiffeners. The contours are presented at different x/H coordinates to highlight the onset of mixing structures in the channel, which are much closer to the inlet than those without stiffeners. Here the unmixed flow occurs until x/H of 10.0, where vortex structures begin to shed from a stiffener, compared to the previous cases where the vortices would originate at a turning corner. Along the membrane surface at x/H before 10.0, a thicker thermal boundary layer is caused by the unmixed flow field. As a result, there are more opportunities for flow separation and for smaller, less homogeneous vortex structures, which is seen in the contours of velocity and vorticity. Contours of vorticity magnitude in the module with stiffeners show a further increase in flow field areas with intense vortical activities than in the module without stiffeners at Re of 2,500. This shows that the vortices induced by flow obstructions, like stiffeners, can provide better mixing than increasing the flow rate in a channel without stiffeners. A dead zone immediately downstream of the stiffeners is shown in the contours of velocity and vorticity. These areas are subject to a higher temperature (and concentration, not shown) polarization than the membrane surface exposed to good mixing. The momentum and thermal boundary layer dissipation can be seen in normalized velocity and temperature contours. Near the membrane surface, there is no perceptible change in temperature compared to the bulk fluid. The iso-surface of the Q-criterion shows much smaller vortex structures more densely packed in the channel with stiffeners than those without. In addition, the vortices are more chaotic, showing that the distribution of the counter/clockwise vortices is more even throughout the channel than the geometry without spacers where the channel is bisected by counter/clockwise turning vortex structures.

Fig. 8 presents line plots along the membrane surface to quantify the effect of geometric and Reynolds number alterations. Results are presented for channels with a (1) flat sheet membrane, (2) wiggly membrane, and (3) wiggly membrane with stiffeners. In the flat modules, the maximum flux is near the inlet region, and as the fluid near the membrane surface vaporizes, heat is lost, and the local temperature decreases, which causes the flux to fall. This temperature decrease can be seen as streamwise (axial) temperature polarization, compared to the crossflow (lateral) polarization based on the extent of the boundary layer and discussed in the contours. In the flat sheet membrane module at Re = 1,500, the normalized temperature drops from 1.0 to 0.95, and the flux decreases from 130 to 50 kg/m^2·h. A 5% difference in the normalized temperature (temperature polarization) caused a 160% decrease in flux in the module. Axial concentration polarization is also seen as pure water diffuses from the solution, where the outlet concentration is higher than the inlet concentration. Minor local membrane temperature and concentration changes can account for significant differences in flux, so mitigating polarizations

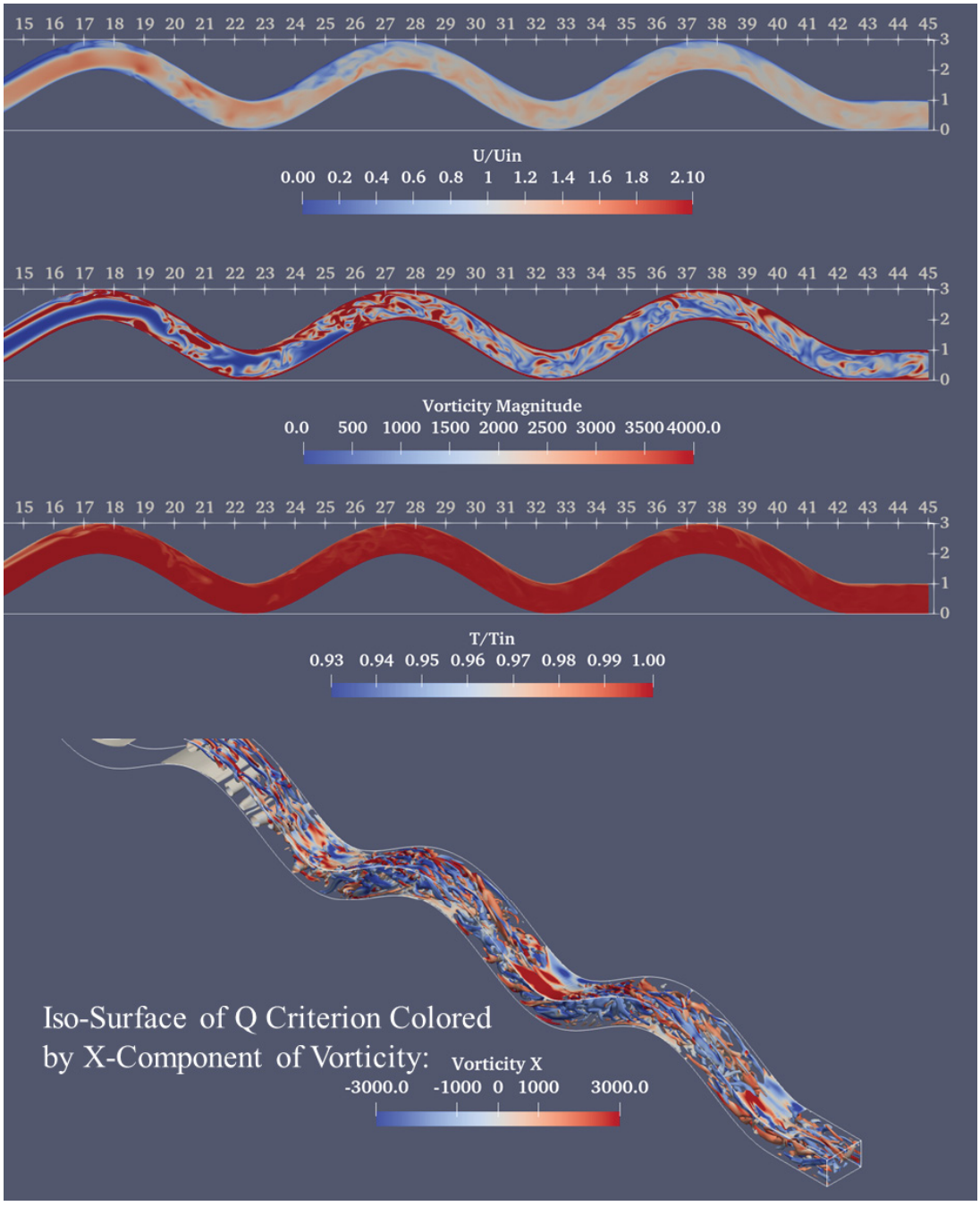

Fig. 6. Midplane contours of (top) normalized velocity (middle) vorticity magnitude (bottom) normalized temperature for Re 2,500 with a sinusoidal channel profile. Midplane corresponds to $z/H = 1.25$.

is essential for successful high-performance separation. Geometric and operational condition changes – increasing the Reynolds number – are utilized to prevent this behavior. For instance, introducing the sinusoidal wall profile at Reynolds number 1,500 provides two distinct flow regions, mixed and unmixed. The unmixed region near the inlet shows a lower normalized membrane temperature and flux than the flat sheet case. After x/H of 22.5, vortices shed in the channel, and flow separation occurs. In this region, there is an increase in performance as the mixing reduces the thermal boundary layer thickness and the membrane's local temperature increases. The length of this region increases at Re = 2,500, where mixing occurs at an earlier corner located at x/H of 17.5. The increased magnitude of mixing can be seen in the higher normalized temperature values. Further enhancement in mixing is shown in the module with the stiffeners, where the mixing structures begin at x/H of 10.0. Thus, more of the membrane has a higher local temperature than any other case and, therefore, higher vapor flux. Similar behavior is seen for concentration polarization, where mixing helps

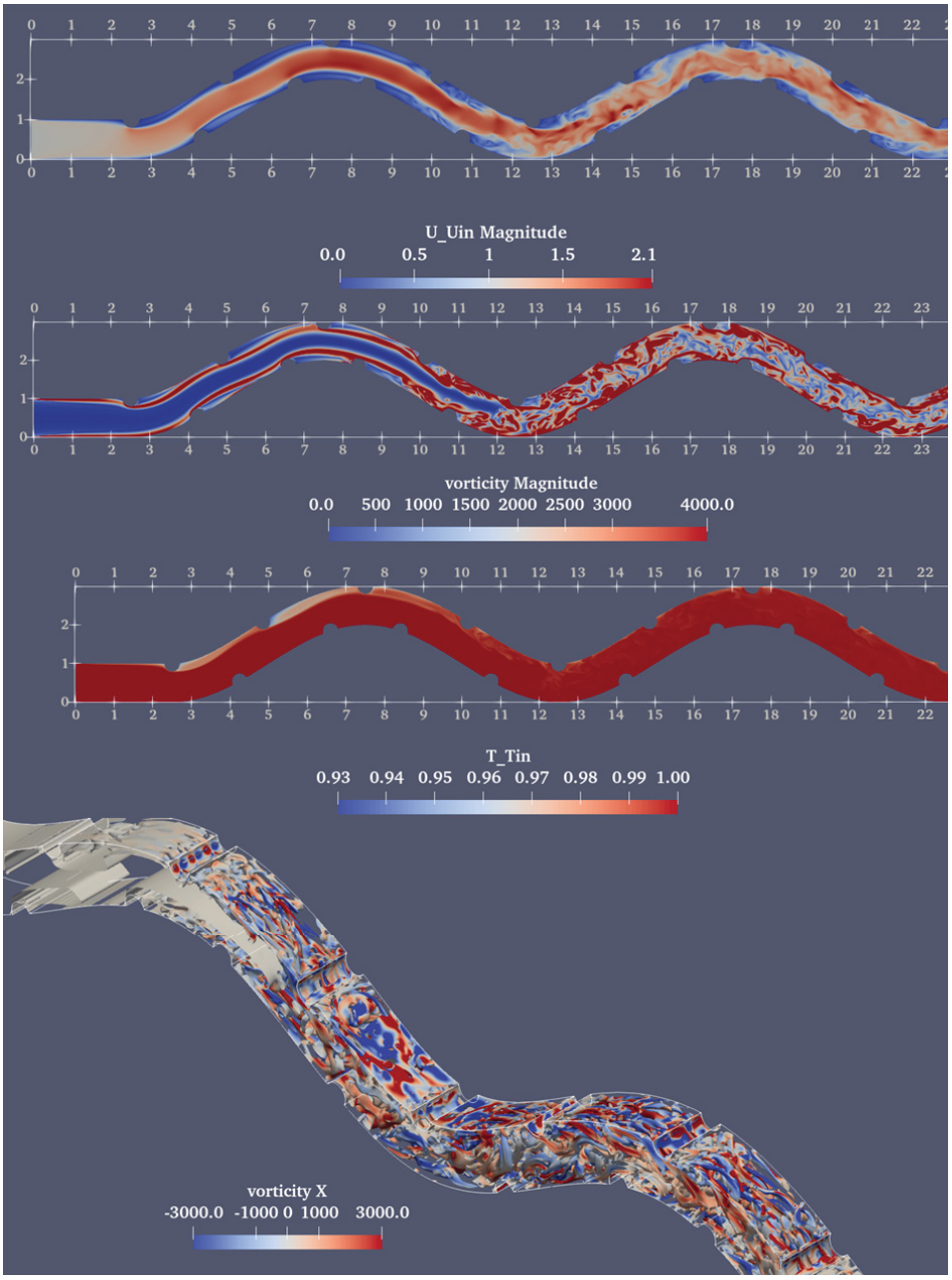

Fig. 7. Midplane contours of (top) normalized velocity (middle) vorticity magnitude (bottom) normalized temperature for Re 1,500 with a sinusoidal channel profile including embedded stiffeners. Midplane corresponds to $z/H = 1.25$.

incorporate bulk solution at lower concentration into the boundary layer- thus reducing the local concentration near the membrane surface. In the mixed region, the effect of axial polarization, or the decrease in flux/temperature with the length, is vastly reduced compared to the flat sheet cases due to the high level of mixing, which is why the vapor flux is higher.

Fig. 9 shows line plots of the Sherwood and Nusselt number along the membrane surface. The Nusselt number represents the ratio of convective heat transfer to conductive heat transfer. Higher values of the Nusselt number imply a better heat exchange rate along the membrane surface. There is a similar analogy to the Sherwood number but for mass transport of the concentration scalar. The Nusselt number is directly related to the membrane heat flux (a linear function of the pure vapor flux through the membrane) and local temperature. Therefore, the Nusselt number strongly correlates to the membrane module's performance metrics, such as temperature polarization and pure vapor flux. Therefore, the distribution of the Nusselt number is similar to the pure vapor flux and normalized temperature. At the beginning of the module, especially in the case without spacers, the Nusselt number is lower in the wiggly cases than the corresponding flat sheet cases. The area of low

performance corresponds to the unmixed region. After the flow separation begins and mixing structures are introduced into the module via vortex shedding, the Nusselt number increases – from around 15 to 25. Shedding occurs at x/H of 22.5 at Reynolds number 1,500 and 17.5 at Reynolds number 2,500. Once in the mixed region, the decay of the Nusselt number with length is much smaller compared to the flat sheet cases. Similar behavior is seen in line plots of the Sherwood number, where there is an increase in the local value after vortex shedding begins.

The averaged values of Nusselt and Sherwood numbers for the cases previously presented are shown in Table 4. By increasing the Reynolds number from 1,500 to 2,500 in the flat sheet case, there is a 33% increase in the Nusselt number. For low Reynolds numbers with mixing in the channel, the Nusselt numbers of the system are similar to those studied by Shakaib et al. [75] (in this case, the wiggly channel was used to promote mixing vortices, in the cited work spacers were considered). As the Reynolds number increases to the transitional flow regime, despite no turbulent structures in the channel, the pressure drop per meter of channel length increases from 4.2 to 11.1 kPa/m. The channel length is given in Fig. 1, varying from 95 to 97 mm to keep the arc length constant, and the results are scaled to kPa/m accordingly. Going from a flat to a wiggly channel increases the Nusselt number by 40% for both Reynolds numbers. The highest Nusselt number is shown in the case with embedded stiffeners, which is indicative of the analysis that having more obstructions in the flow and creating mixing structures throughout the whole channel, instead of close to the outlet region, will better facilitate heat transfer in the channel and lead to a higher temperature and corresponding vapor flux along the membrane surface. Because some energy in the flow is dissipated with mixing structures, the pressure drop in the module increases with increasing Nusselt number, as

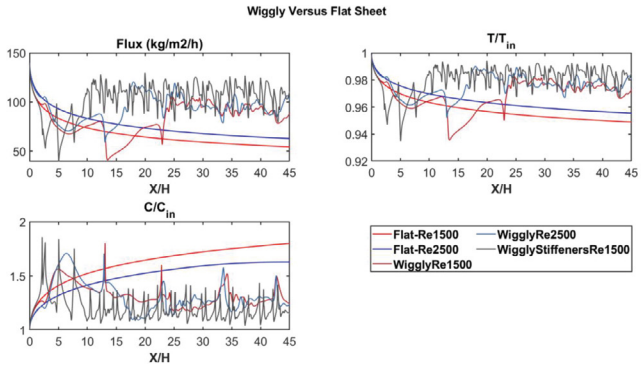

Fig. 8. Line profiles along the midplane of the membrane surface at the final time step for flux, normalized temperature, and normalized concentration for 3D LES simulations with geometry specified in Fig. 1. Midplane corresponds to $z/H = 1.25$.

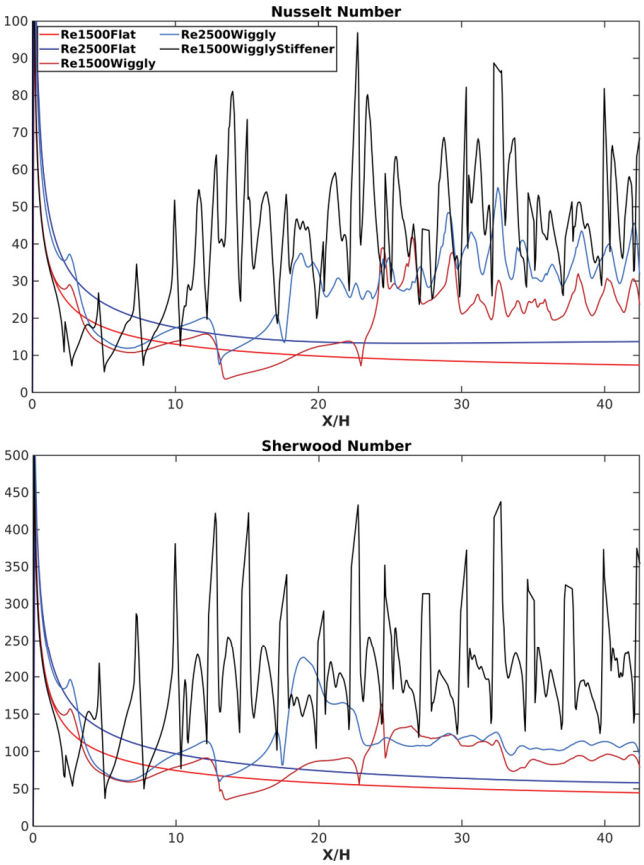

Fig. 9. Line profiles along the midplane of the membrane surface at the final time step for (top) Nusselt number (bottom) Sherwood number for LES simulations with geometry specified in Fig. 1. Midplane corresponds to $z/H = 1.25$.

Table 4
Final table of results for all cases taking module averaged values using instantaneous data gathered from the final timestep. Note the Reynolds number 1,500 cases have a boldfaced merit criterion to denote one baseline case vs. the Reynolds number 2,500 cases which use italics to denote a different baseline. The reference values under the case column for the flat channels are also bolded/italicized depending on the Reynolds number. Pressure drop is scaled to a module length of 1 m long

Case	Average Nusselt number	Average Sherwood number	Static pressure drop ($\Delta P/\Delta X$ = kPa·m)	Friction factor	Merit criterion
Re 1,500 flat	11.7	66.3	4.2	0.0298	**1.0**
Re 2,500 flat	17.4	85.6	11.1	0.0284	1.0
Re 1,500 wiggly	19.9	93.0	7.6	0.0538	**1.40**
Re 2,500 wiggly	29.0	118.8	17.9	0.0458	1.42
Re 1,500 wiggly stiffener	41.7	194.7	24.6	0.175	**1.97**

more vortices will yield a higher pressure drop and better heat transfer. Note that the feed solution is at atmospheric pressure in vacuum membrane distillation. The permeate stream is held at 5 kPa in these simulations. This pressure difference can be compared against the 6,000–8,000 kPa range a reverse osmosis module is designed for [76], eliminating the need for a complex pressure vessel in VMD and high-pressure pumps and pressure recovery systems, therefore reducing system complexity. The pressure drops are similar to those measured by Xie et al. [77], who studied a similar channel profile for reverse osmosis using computational fluid dynamics.

The pressure drop is critical for determining whether the membrane experiences wetting in membrane distillation processes. Vacuum membrane distillation is more prone to wetting due to the vacuum on the permeate side, which is why typical vacuum membranes use a 0.2 μm pore diameter vs. a 0.45 μm diameter popular in direct contact, air gap, and sweeping gas membrane distillation. Partial pore wetting can occur at lower than the liquid entry pressure based on an uneven pore distribution. The pressure difference across the membrane is a function of the partial vapor pressure and the feed pressure (in this case, ambient pressure at 101.3 kPa, although other studies have considered pressurized feed solutions to increase the temperature difference without boiling the feed [78], utilizing a feed pressure of 910–1,500 kPa). For the considered modules having a 95 mm channel length, the transmembrane pressure difference, including the pressure drop, is below the minimum value of the liquid entry pressure. However, extrapolating to a 1-m channel length, as done in Table 4, the transmembrane pressure difference exceeds 100 kPa. Existing prototype scale VMD modules typically operate without mixing structures, based on a low incoming mass flow rate or hollow fibers with a small hydraulic diameter compared to an empty membrane channel. This helps maintain a lower pressure drop and, therefore, less propensity to wetting (same with adjustments to the vacuum pressure). Calculating the pressure drop shows the critical importance of using CFD studies to understand the hydrodynamics of the channel, as high-performing modules with vortex mixing will suffer increased pressure drop. There is also an essential coupling of CFD studies with membrane science in order to manufacture membranes with large contact angles and corresponding high liquid entry pressures, as well as low variance in the pore size distribution to prevent failure from partial/full pore wetting.

The pressure drop values are used to calculate the friction factor for each channel. Then, using the friction factors and Nusselt numbers, a merit criterion was defined for each Reynolds number, using the flat sheet cases as baselines. Note the Reynolds number 1,500 cases have a boldfaced merit criterion to denote one baseline case vs. the Reynolds number 2,500 cases which use italics to denote a different baseline. In this case, increasing changing from a flat to a wiggly geometry increased the system performance (evaluated by merit criterion) by 40% of the baseline, and embedding stiffeners in the membrane increased the system merit by 97% compared to the baseline, showing the geometric alterations outstripped only increasing the Reynolds number, and the value of using embedded stiffeners along with morphological changes in the channel.

The effect of the wiggly geometry, flow rate, and stiffeners have been presented in Figs. 4–9 using 3D LES simulation for a wiggly channel with x/H of 45. One of the critical issues with membrane distillation is transitioning from a lab-scale system to an industrial scale. The computational expense of conducting LES simulations to resolve the flow field for these lab-scale units is significant. One way of minimizing this is to conduct simulations using a 2D geometry. 2D LES simulations have also been run in the wiggly membrane with/out embedded stiffeners at Reynolds number 1,500 to compare results obtained in the corresponding 3D geometry. Fig. 10 shows line plots of instantaneous fluid properties along the membrane surface at the final time step.

The significant difference between 2D and 3D is in the concentration. One reason for this could be that the mesh cells are much smaller in the 2D case to gain extra resolution. For reference, 20 million finite volume cells were used in the 3D geometry, whereas 4 million cells were utilized in the 2D geometry without stiffeners. For the geometry with stiffeners, 33 million cells were used in 3D vs. 1 million for the 2D geometry. The 2D mesh cell size is more refined in all cases than the 3D mesh. The cell size showed a smaller decrease in the channel with stiffeners, resulting in a similar concentration distribution at the final time step. Based on the temperature and flux readings, the authors can claim that the 2D simulations are an acceptable approximation to study the flux behavior of the channel. Therefore, a new set of 2D geometries, as shown in Fig. 11, are considered to extend the present study to more extended length channels to study length degradation in VMD modules.

The line profiles along the membrane surface for the final time step using the extended computational domain are shown in Fig. 12. The first thing to note is that regardless of the channel length, the distance from the inlet where the mixed regime begins is the same; for example, mixing structures still appear at x/H of 10.0 in the geometry with stiffeners. With the longer channel, it's easier to see the effect of axial polarizations. The flux value decreases along the channel length as heat and pure water exit the feed solution, and the temperature falls while the concentration rises. In the unmixed region, there are regions near turning corners

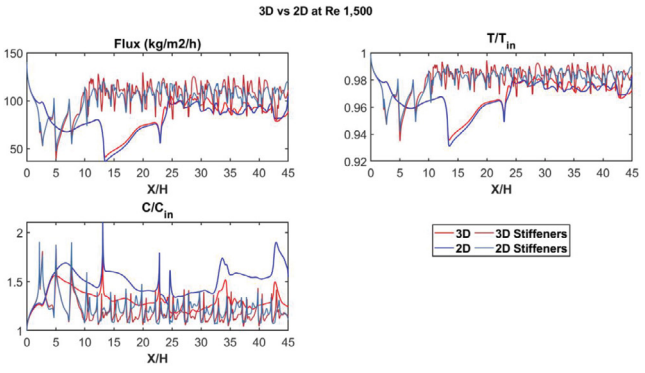

Fig. 10. Line profiles along the midplane of the membrane surface for 2D vs. 3D cases at a fixed Reynolds number presenting: flux, normalized temperature, and normalized concentration with the wiggly geometry specified in Fig. 1. 3D Midplane corresponds to $z/H = 1.25$.

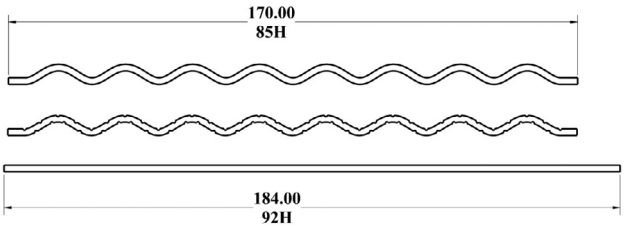

Fig. 11. The 2D computational domain for the long wiggly (with and without stiffeners) and flat sheet membrane. Dimensions in mm. The membrane surface area is kept constant.

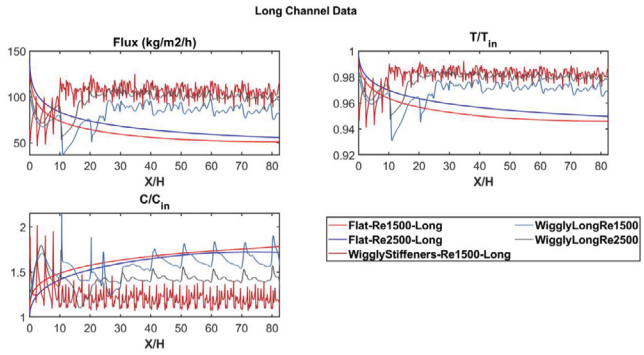

Fig. 12. Line profiles along the midplane of the membrane surface at the final time step for flux, normalized temperature, and normalized concentration for 3D LES simulations with geometry specified in Fig. 1. Midplane corresponds to $z/H = 1.25$.

corresponding to the areas where fluid is pushed away from the membrane, and these areas show poor performance. The flux and temperature decline in the presence of mixing structures is less than the flat sheet geometry, even in the case of the more extended channel. Furthermore, stiffeners yielded much higher performance for a Reynolds number of 1,500 than a wiggly case without flow obstructions at Reynolds number 2,500, showing the effect of turbulators vs. the operational conditions. This is because the higher level of mixing provided by the stiffeners (shown in the vorticity contours and iso-surfaces for a 3D case at a shorter length) alleviates the temperature polarization along the membrane surface more effectively than simply increasing the Reynolds number.

The results for both the short 3D and long 2D geometries are presented in Table 5. The module temperature and concentration polarization coefficient (TPC and CPC, respectively) represent the average value of the normalized temperature and concentration. The values are gathered using information from the final time step of the simulation.

The effect of changing the geometry can be seen in the Reynolds number 1,500 cases, where a flat, wiggly, and wiggly with stiffeners geometry was considered. Compared to the baseline, flat sheet geometry, for the short channel, there is a 25% increase in the flux when changing to the wiggly geometry and a 56% increase in flux when changing to the wiggly and stiffeners geometry. These significant (around 50%) increases in flux associated with enhanced mixing are seen in existing membrane distillation literature, such as

Table 5
Final table of results for all cases taking module averaged values using instantaneous data gathered from the final timestep

Case	Flux	TPC	CPC
Short ($x/H = 45$)			
Re 1,500-flat	66.3	0.956	1.64
Re 2,500-flat	75.2	0.964	1.51
Re 1,500 - Wiggly	82.8	0.969	1.32
Re 2,500 - Wiggly	93.5	0.975	1.31
Re 1,500 – Wiggly + Stiffeners	103.1	0.981	1.20
Long ($x/H = 85$)			
Re 1,500-flat	59.3	0.952	1.66
Re 2,500-flat	66.8	0.958	1.61
Re 1,500 - Wiggly	82.3	0.969	1.56
Re 2,500 - Wiggly	97.4	0.978	1.41
Re 1,500 – Wiggly + Stiffeners	103.4	0.981	1.22

Thomas et al. [28] and Alwatban et al. [42]. However, when changing from flat sheet case at Reynolds number 1,500 to 2,500, there is only a 14% increase. These increases in flux are attributed to the decrease in temperature and concentration polarization caused by the induced mixing structures. It is shown in the third and fourth columns where, compared against the flat sheet case, the wiggly with stiffeners shows a 2% variance in the module averaged temperature polarization coefficient, and that minor difference accounts for a significant increase in the flux performance. Similarly, the concentration build-up local to the membrane surface is also reduced by a much larger margin, which isn't reflected in the flux performance. Table 4 shows the Nusselt and Sherwood numbers in the system; the flux and temperature/concentration polarization don't increase linearly with increasing Nusselt/Sherwood numbers. This is because the temperature drop decreases in the channel, and the heat flux (corresponding to pure vapor flux) increases with geometric changes, so several changes are affecting the Nusselt number calculation.

In addition to increasing the performance in the short channel by mitigating the effect of the lateral temperature polarization caused by reducing the effect of the thermal boundary layer on the membrane, there are also axial temperature polarization reductions. These can be shown by comparing the short- and long-channel results. The effect of axial polarization is seen in the flat sheet cases, where the flux decreases with increasing length. Depending on the Reynolds number, the flux decreases 10%–13% as the length increases. However, that reduction in flux is eliminated in all cases due to good mixing induced by geometric alterations. Since the results are presented at a single time step, in some cases, the extended channel flux is greater than the short channel flux, but time averaging would eliminate that disparity. Time averaging wasn't utilized for the table because it would cause inconsistent instantaneous line plots presented above and the module-averaged properties. Animations in the supplementary document highlight the transient nature of the module.

4. Conclusion

3D and 2D large eddy simulations on vacuum membrane distillation modules were conducted to resolve the transient flow field and the module performance. The parameters considered included changes to the channel geometry and the flow rate. A Reynolds number of 1,500 and 2,500 were considered for a flat sheet membrane, a wiggly membrane, and a wiggly membrane with embedded stiffeners. Two distinct regimes were seen in the flow field: unmixed and mixed. The unmixed regime is close to the inlet and resembles the steady-state solution with a parabolic velocity profile in the channel. Further downstream, there is a transition around a turning corner or stiffener, where vortex activity begins. These structures mix the hot bulk solution at low concentration into the boundary layer close to the membrane, reducing temperature and concentration polarization. The Nusselt and Sherwood number was post-processed to determine the effectiveness of the geometric alterations on heat/mass transfer. Compared to the base case, the Nusselt number showed a 250% increase from 11.7 to 41.7. Defining a merit criterion using the Nusselt numbers and friction factors showed a 40% increase in merit regardless of the Reynolds number going from a flat to a wiggly channel. A 97% increase in merit was seen when stiffeners were included in the channel. The vorticity magnitude increases with the Reynolds number and with adding stiffeners to the channel, and the strength of the mixing corresponds closely to the reduction in polarization. As the vorticity magnitude increased, the structures in the channel became smaller and more chaotic. The areas inside the module with the highest flux performance and lowest temperature polarization correspond to the mixed regime. Overall, the geometric changes contributed to a 56% increase in the flux performance for the short channel going from a flat sheet membrane to a wiggly channel with stiffeners at Reynolds number 1,500. A 42% flux improvement went from the base case to a wiggly case at Reynolds number 2,500. In this instance, increasing the Reynolds number but removing the stiffeners leads to a lesser flux improvement, showing that a combination of a smartly chosen flow rate and geometric alterations to promote mixing are critical to achieving peak flux performance in a membrane distillation module. In addition, simulations were extended to channels of longer lengths using 2D geometries. In the longer length, the flat sheet membrane geometries showed a flux decline of 13% due to the buildup of axial temperature polarization. The wiggly geometries mitigate that, proving that the geometric alterations to induce turbulence effectively prevent the performance decrease with increasing membrane area. These results highlight the importance of understanding how to effectively scale up membrane distillation systems and some issues that can arise as the modules are extended in the streamwise direction.

Acknowledgment

This work was sponsored by the US Department of Energy under the Advanced Manufacturing Office Grant DE-EE0009735 for the Industrial Assessment Center at Lehigh University. In addition, this work is used supported by the National Science Foundation grant number 2019035. Finally, this work used the National Science Foundation grant number ACCESS MCH220041—specifically, the Bridges-2 system at the Pittsburgh Supercomputing Center.

References

[1] UN Water, Sustainable Development Goal 6 Synthesis Report on Water and Sanitation, 2018.
[2] E. Jones, M. Qadir, M.T.H. van Vliet, V. Smakhtin, S. mu Kang, The state of desalination and brine production: a global outlook, Sci. Total Environ., 657 (2019) 1343–1356.
[3] N. Ghaffour, T.M. Missimer, G.L. Amy, Technical review and evaluation of the economics of water desalination: current and future challenges for better water supply sustainability, Desalination, 309 (2013) 197–207.
[4] C. Skuse, A. Gallego-Schmid, A. Azapagic, P. Gorgojo, Can emerging membrane-based desalination technologies replace reverse osmosis?, Desalination, 500 (2021) 114844, doi: 10.1016/j.desal.2020.114844.
[5] N. Voutchkov, Energy use for membrane seawater desalination – current status and trends, Desalination, 431 (2018) 2–14.
[6] S. Al-Obaidani, E. Curcio, F. Macedonio, G. Di Profio, H. Al-Hinai, E. Drioli, Potential of membrane distillation in seawater desalination: thermal efficiency, sensitivity study and cost estimation, J. Membr. Sci., 323 (2008) 85–98.
[7] M. Khayet, Solar desalination by membrane distillation: dispersion in energy consumption analysis and water production costs (a review), Desalination, 308 (2013) 89–101.
[8] D. Winter, J. Koschikowski, F. Gross, D. Maucher, D. Düver, M. Jositz, T. Mann, A. Hagedorn, Comparative analysis of full-scale membrane distillation contactors – methods and modules, J. Membr. Sci., 524 (2017) 758–771.
[9] M. Jafari, M. Vanoppen, J.M.C. van Agtmaal, E.R. Cornelissen, J.S. Vrouwenvelder, A. Verliefde, M.C.M. van Loosdrecht, C. Picioreanu, Cost of fouling in full-scale reverse osmosis and nanofiltration installations in the Netherlands, Desalination, 500 (2021) 114865, doi: 10.1016/j.desal.2020.114865.
[10] D. González, J. Amigo, F. Suárez, Membrane distillation: perspectives for sustainable and improved desalination, Renewable Sustainable Energy Rev., 80 (2017) 238–259.
[11] M. Laqbaqbi, M.C. García-Payo, M. Khayet, J. El Kharraz, M. Chaouch, Application of direct contact membrane distillation for textile wastewater treatment and fouling study, Sep. Purif. Technol., 209 (2019) 815–825.
[12] M.O. Mavukkandy, C.M. Chabib, I. Mustafa, A. Al Ghaferi, F. AlMarzooqi, Brine management in desalination industry: from waste to resources generation, Desalination, 472 (2019) 114187, doi: 10.1016/j.desal.2019.114187.
[13] R.B. Lakeh, C. Salerno, E.P. Herlim, J. Kiriakos, S. Delagah, Repurposing reverse osmosis concentrate as a low-cost thermal energy storage medium, J. Clean Energy Technol., 8 (2020) 31–40.
[14] A.M. Alwatban, A.M. Alshwairekh, U.F. Alqsair, A.A. Alghafis, A. Oztekin, Effect of membrane properties and operational parameters on systems for seawater desalination using computational fluid dynamics simulations, Desal. Water Treat., 161 (2019) 92–107.
[15] M. Qtaishat, T. Matsuura, B. Kruczek, M. Khayet, Heat and mass transfer analysis in direct contact membrane distillation, Desalination, 219 (2008) 272–292.
[16] B. Li, K.K. Sirkar, Novel membrane and device for direct contact membrane distillation-based desalination process, Ind. Eng. Chem. Res., 43 (2004) 5300–5309
[17] L. Eykens, T. Reyns, K. De Sitter, C. Dotremont, L. Pinoy, B. Van der Bruggen, How to select a membrane distillation configuration? Process conditions and membrane influence unraveled, Desalination, 399 (2016) 105–115.
[18] U.F. Alqsair, A. Alshwairekh, A.M. Alwatban, A. Oztekin, Computational study of sweeping gas membrane distillation process – flux performance and polarization characteristics, Desalination, 485 (2020) 114444, doi: 10.1016/j.desal.2020.114444.

[19] M. Khayet, P. Godino, J.I. Mengual, Nature of flow on sweeping gas membrane distillation, J. Membr. Sci., 170 (2000) 243–255.
[20] M. Khayet, T. Matsuura, Pervaporation and vacuum membrane distillation processes: modeling and experiments, AlChE J., 50 (2004) 1697–1712.
[21] J.G. Lee, W.S. Kim, Numerical modeling of the vacuum membrane distillation process, Desalination, 331 (2013) 46–55.
[22] M. Usta, Computational Study of Desalination by Membranes, Lehigh University, 2018. Available at: https://preserve.lehigh.edu/etd/4328%0AThis
[23] G. Rácz, S. Kerker, Z. Kovács, G. Vatai, M. Ebrahimi, P. Czermak, Theoretical and experimental approaches of liquid entry pressure determination in membrane distillation processes, Period. Polytech., Chem. Eng., 58 (2014) 81–91.
[24] M.R. Choudhury, N. Anwar, D. Jassby, M.S. Rahaman, Fouling and wetting in the membrane distillation driven wastewater reclamation process – a review, Adv. Colloid Interface Sci., 269 (2019) 370–399.
[25] D.M. Warsinger, J. Swaminathan, E. Guillén-Burrieza, H.A. Arafat, J.H. Lienhard V, Scaling and fouling in membrane distillation for desalination applications: a review, Desalination, 356 (2015) 294–313.
[26] Y. Zhang, Y. Peng, S. Ji, S. Wang, Numerical simulation of 3D hollow-fiber vacuum membrane distillation by computational fluid dynamics, Chem. Eng. Sci., 152 (2016) 172–185.
[27] Q. Li, B. Lian, W. Zhong, A. Omar, A. Razmjou, P. Dai, J. Guan, G. Leslie, R.A. Taylor, Improving the performance of vacuum membrane distillation using a 3D-printed helical baffle and a superhydrophobic nanocomposite membrane, Sep. Purif. Technol., 248 (2020) 117072, doi: 10.1016/j.seppur.2020.117072.
[28] N. Thomas, N. Sreedhar, O. Al-Ketan, R. Rowshan, R.K. Abu Al-Rub, H.A. Arafat, 3D printed triply periodic minimal surfaces as spacers for enhanced heat and mass transfer in membrane distillation, Desalination, 443 (2018) 256–271.
[29] R.W. Schofield, A.G. Fane, C.J.D. Fell, R. Macoun, Factors affecting flux in membrane distillation, Desalination, 77 (1990) 279–294.
[30] B. Li, K.K. Sirkar, Novel membrane and device for vacuum membrane distillation-based desalination process, J. Membr. Sci., 257 (2005) 60–75.
[31] A.S. Kim, H.S. Lee, D.S. Moon, H.J. Kim, Self-adjusting, combined diffusion in direct contact and vacuum membrane distillation, J. Membr. Sci., 543 (2017) 255–268.
[32] V. Soni, J. Abildskov, G. Jonsson, R. Gani, Modeling and analysis of vacuum membrane distillation for the recovery of volatile aroma compounds from black currant juice, J. Membr. Sci., 320 (2008) 442–455.
[33] H. Ji, M.Y. Choi, H.S. Lee, A.S. Kim, H.J. Kim, Vacuum membrane distillation for deep seawater: experiments and theory, Desal. Water Treat., 58 (2017) 344–350.
[34] Y. Zhang, Y. Peng, S. Ji, Z. Li, P. Chen, Review of thermal efficiency and heat recycling in membrane distillation processes, Desalination, 367 (2015) 223–239.
[35] Y. Wang, Z. Xu, N. Lior, H. Zeng, An experimental study of solar thermal vacuum membrane distillation desalination, Desal. Water Treat., 53 (2015) 887–897.
[36] G. Zaragoza, J.A. Andrés-Mañas, A. Ruiz-Aguirre, Commercial scale membrane distillation for solar desalination, npj Clean Water, 1 (2018) 20, doi: 10.1038/s41545-018-0020-z.
[37] F. Kiefer, M. Spinnler, T. Sattelmayer, Multi-effect vacuum membrane distillation systems: model derivation and calibration, Desalination, 438 (2018) 97–111.
[38] E.S. Mohamed, P. Boutikos, E. Mathioulakis, V. Belessiotis, Experimental evaluation of the performance and energy efficiency of a vacuum multi-effect membrane distillation system, Desalination, 408 (2017) 70–80.
[39] A. Luo, N. Lior, Critical review of membrane distillation performance criteria, Desal. Water Treat., 57 (2016) 20093–20140.
[40] M.F. Gruber, U. Aslak, C. Hélix-Nielsen, Open-source CFD model for optimization of forward osmosis and reverse osmosis membrane modules, Sep. Purif. Technol., 158 (2016) 183–192.
[41] M.F. Gruber, C.J. Johnson, C. Tang, M.H. Jensen, L. Yde, C. Helix-Nielsen, Validation and analysis of forward osmosis CFD model in complex 3D geometries, Membranes (Basel), 2 (2012) 764–782.
[42] A.M. Alwatban, A.M. Alshwairekh, U.F. Alqsair, A.A. Alghafis, A. Oztekin, Performance improvements by embedded spacer in direct contact membrane distillation – computational study, Desalination, 470 (2019) 114103, doi: 10.1016/j.desal.2019.114103.
[43] A.E. Anqi, M. Usta, R. Krysko, J.-G. Lee, N. Ghaffour, A. Oztekin, Numerical study of desalination by vacuum membrane distillation – transient three-dimensional analysis, J. Membr. Sci., 596 (2020) 117609, doi: 10.1016/j.memsci.2019.117609.
[44] J. Amigo, R. Urtubia, F. Suárez, Exploring the interactions between hydrodynamics and fouling in membrane distillation systems – a multiscale approach using CFD, Desalination, 444 (2018) 63–74.
[45] Z. Zhou, B. Ling, I. Battiato, S.M. Husson, D. Ladner, Concentration polarization over reverse osmosis membranes with engineered surface features, J. Membr. Sci., 617 (2021) 118199, doi: 10.1016/j.memsci.2020.118199.
[46] M. Usta, A. Anqi, A. Oztekin, Reverse osmosis desalination modules containing corrugated membranes – computational study, Desalination, 416 (2017) 129–139.
[47] X. Yang, H. Yu, R. Wang, A.G. Fane, Optimization of microstructured hollow fiber design for membrane distillation applications using CFD modeling, J. Membr. Sci., 421–422 (2012) 258–270.
[48] M.A. Abdulhamid, S.-H. Park, Z. Zhou, D. Ladner, G. Szekely, Surface engineering of intrinsically microporous poly(ether-ether-ketone) membranes: from flat to honeycomb structures, J. Membr. Sci., 621 (2021) 118997, doi: 10.1016/j.memsci.2020.118997.
[49] M. Gryta, The application of submerged modules for membrane distillation, Membranes (Basel), 10 (2020) 7–10.
[50] J.P. Mericq, S. Laborie, C. Cabassud, Vacuum membrane distillation for an integrated seawater desalination process, Desal. Water Treat., 9 (2009) 287–296.
[51] P. Tiwari, S.P. Antal, A. Burgoyne, G. Belfort, M.Z. Podowski, Multifield computational fluid dynamics model of particulate flow in curved circular tubes, Theor. Comput. Fluid Dyn., 18 (2004) 205–220.
[52] S. Acharya, S.K. Dash, Natural convection heat transfer from a short or long, solid or hollow horizontal cylinder suspended in air or placed on ground, J. Heat Transfer, 139 (2017), doi: 10.1115/1.4035919.
[53] E. Salcedo, J.C. Cajas, C. Treviño, L. Martínez-Suástegui, Numerical investigation of mixed convection heat transfer from two isothermal circular cylinders in tandem arrangement: buoyancy, spacing ratio, and confinement effects, Theor. Comput. Fluid Dyn., 31 (2017) 159–187.
[54] R. Zhang, Y. Liu, M. He, Y. Su, X. Zhao, M. Elimelech, Z. Jiang, Antifouling membranes for sustainable water purification: strategies and mechanisms, Chem. Soc. Rev., 45 (2016) 5888–5924.
[55] M. Khayet, J.I. Mengual, T. Matsuura, Porous hydrophobic/hydrophilic composite membranes: application in desalination using direct contact membrane distillation, J. Membr. Sci., 252 (2005) 101–113.
[56] K.J. Lu, D. Zhao, Y. Chen, J. Chang, T.-S. Chung, Rheologically controlled design of nature-inspired superhydrophobic and self-cleaning membranes for clean water production, npj Clean Water, 3 (2020) 30, doi: 10.1038/s41545-020-0078-2.
[57] P. Xie, L.C. Murdoch, D. Ladner, Mitigating membrane fouling with sinusoidal spacers, Desal. Water Treat., 168 (2019) 56–64.
[58] B. Ling, P. Xie, D. Ladner, I. Battiato, Dynamic modeling of fouling in reverse osmosis membranes, Membranes (Basel), 11 (2021) 349, doi: 10.3390/membranes11050349.
[59] D. Winter, J. Koschikowski, M. Wieghaus, Desalination using membrane distillation: experimental studies on full scale spiral wound modules, J. Membr. Sci., 375 (2011) 104–112.
[60] A. Hagedorn, G. Fieg, D. Winter, J. Koschikowski, T. Mann, Methodical design and operation of membrane distillation

plants for desalination, Chem. Eng. Res. Des., 125 (2017) 265–281.
[61] E. Guillén-Burrieza, J. Blanco, G. Zaragoza, D.C. Alarcón, P. Palenzuela, M. Ibarra, W. Gernjak, Experimental analysis of an air gap membrane distillation solar desalination pilot system, J. Membr. Sci., 379 (2011) 386–396.
[62] H.S. Son, M.W. Shahzad, N. Ghaffour, K.C. Ng, Pilot studies on synergetic impacts of energy utilization in hybrid desalination system: multi-effect distillation and adsorption cycle (MED-AD), Desalination, 477 (2020) 114266, doi: 10.1016/j.desal.2019.114266.
[63] S. Gabsi, N. Frikha, B. Chaouachi, Performance of a solar vacuum membrane distillation pilot plant, for seawater desalination in Mahares, Tunisia, Int. J. Water Resour. Arid Environ., 2 (2013) 213–217.
[64] S. Ben Abdallah, N. Frikha, S. Gabsi, Design of an autonomous solar desalination plant using vacuum membrane distillation, the MEDINA project, Chem. Eng. Res. Des., 91 (2013) 2782–2788.
[65] H.C. Duong, A.R. Chivas, B. Nelemans, M. Duke, S. Gray, T.Y. Cath, L.D. Nghiem, Treatment of RO brine from CSG produced water by spiral-wound air gap membrane distillation — a pilot study, Desalination, 366 (2015) 121–129.
[66] R.W. Schofield, Membrane Distillation, The University of New South Wales, 1989.
[67] B.E. Poling, J.M. Prausnitz, J.P. O'Connell, Properties of Gases and Liquids, 5th ed., McGraw-Hill Education, New York, Chicago, San Francisco, Athens, London, Madrid, Mexico City, Milan, New Delhi, Singapore, Sydney, Toronto, 2001.
[68] K.W. Lawson, D.R. Lloyd, Review membrane distillation, J. Membr. Sci., 124 (1997) 1–25.
[69] R.D. Present, Kinetic Theory of Gases, McGraw-Hill, New York, 1958.
[70] T. Matsuura, Synthetic Membranes and Membrane Separation Processes, CRC Press, Boca Raton, 1994. Available at: https://doi.org/10.1201/9781003068037.
[71] M. Khayet, Membranes and theoretical modeling of membrane distillation: a review, Adv. Colloid Interface Sci., 164 (2011) 56–88.
[72] L. Martínez, F.J. Florido-Díaz, A. Hernández, P. Prádanos, Characterisation of three hydrophobic porous membranes used in membrane distillation: modelling and evaluation of their water vapour permeabilities, J. Membr. Sci., 203 (2002) 15–27.
[73] M. La Cerva, M. Ciofalo, L. Gurreri, A. Tamburini, A. Cipollina, G. Micale, On some issues in the computational modelling of spacer-filled channels for membrane distillation, Desalination, 411 (2017) 101–111.
[74] M. Usta, R.M. Krysko, A. Anqi, A. Alshwairekh, A. Oztekin, The Effect of PTFE Membrane Properties on Vacuum Membrane Distillation Module Performance, Conference: 2018 International Mechanical Engineering Congress and Exposition, Pittsburgh, PA, 2018. Available at: https://doi.org/10.1115/imece2018-86327
[75] M. Shakaib, S.M.F. Hasani, I. Ahmed, R.M. Yunus, A CFD study on the effect of spacer orientation on temperature polarization in membrane distillation modules, Desalination, 284 (2012) 332–340.
[76] D.M. Davenport, A. Deshmukh, J.R. Werber, M. Elimelech, High-pressure reverse osmosis for energy-efficient hypersaline brine desalination: current status, design considerations, and research needs, Environ. Sci. Technol. Lett., 5 (2018) 467–475.
[77] P. Xie, L.C. Murdoch, D. Ladner, Hydrodynamics of sinusoidal spacers for improved reverse osmosis performance, J. Membr. Sci., 453 (2014) 92–99.
[78] A. Luo, N. Lior, Study of advancement to higher temperature membrane distillation, Desalination, 419 (2017) 88–100.

Supporting information

S1: Mathematical modeling-LES turbulence modeling

The LES turbulence model was considered to capture the unsteady flow because turbulent structures are present in the channel at high Reynolds numbers. The WALE subgrid model is used to model eddies smaller than the grid size, while all other eddies are directly solved. The LES filtered momentum equation can be written as:

$$\frac{\partial \bar{U}_i}{\partial t} + \bar{U}_j \frac{\partial \bar{U}_i}{\partial x_j} = -\frac{\partial \bar{\bar{p}}}{\partial x_i} - \frac{\partial \overline{\tau_{ij}}}{\partial x_i} + \nu \frac{\partial}{\partial x_j}\left(\frac{\partial \bar{U}_i}{\partial x_j}\right) \tag{S1}$$

where the overbar notation represents the filtering operation. The closure is obtained by modeling the subgrid-scale stress tensor, τ_{ij}, where the relation from the subgrid-scale stress to the large-scale strain rate tensor uses an eddy viscosity model and is given as:

$$\tau_{ij} - \frac{\delta_{ij}}{3}\tau_{kk} = -2\nu_t \overline{S_{ij}} \tag{S2}$$

For the WALE model, the eddy viscosity is given as:

$$\nu_t = \left(C_w \Delta\right)^2 \frac{\left(S_{ij}^d S_{ij}^d\right)^{\frac{3}{2}}}{\left(\overline{S_{ij}^d S_{ij}^d}\right)^{\frac{5}{2}} + \left(S_{ij}^d S_{ij}^d\right)^{\frac{5}{4}}} \tag{S3}$$

Where:

$$S_{ij}^d = \frac{1}{2}\left(\bar{g}_{ij}^2 + \bar{g}_{ji}^2\right) - \frac{\delta_{ij}}{3}\bar{g}_{kk}^2 \tag{S4}$$

$$\bar{g}_{ij} = \frac{\partial \bar{U}_i}{\partial x_i} \tag{S5}$$